Published by IOP Publishing for Sissa Medialab

Received: *February 23, 2026*
Accepted: *March 22, 2026*
Published: *May 5, 2026*

Crystals to assist the two-beam merging process in the UA9-apparatus

W. Scandale,[a,*] **S. Giroldi**,[a] **G. Hall**,[a] **M. Pesaresi**,[a] **R. Rossi**,[a] **K. Uchida**,[a] **F. Cerutti**,[b] **L.S. Esposito**,[b] **S. Gilardoni**,[b] **R. Losito**,[b] **F. Galluccio**,[c] **D. Annucci**,[d] **M. Bauce**,[d] **F. Collamati**,[d] **P. Valente**,[d] **A. Variola**[d] **and S. Di Gennaro**[e]

[a] *Blackett Laboratory, Imperial College, London SW7 2AZ, U.K.*
[b] *European Organization for Nuclear Research CERN, 1211 Geneva 23, Switzerland*
[c] *INFN Sezione di Napoli, Complesso Universitario di Monte Sant'Angelo, Via Cintia, 80126 Napoli, Italy*
[d] *INFN Sezione di Roma, Piazzale Aldo Moro 2, 00185 Rome, Italy*
[e] *Scuola Politecnica e delle Scienze di Base, Università degli Studi di Napoli "Federico II", Via Claudio 21, 80125 Napoli, Italy*

E-mail: Walter.Scandale@cern.ch

Abstract: The UA9 Collaboration proposes to investigate a two-beam merging process aided by bent crystals in an improved version of an apparatus configured for the H8 beam line at the CERN-SPS North Area. The process involves generating two converging beams which combine inside a curved crystal. The resulting beam should include nearly all the incoming particles and to have a horizontal size almost equivalent to the sum of the converging beams. In practice, the combined beam is formed by horizontal stacking of the two original beams, with no active magnetic elements. Crystals shaped like a C, bent by two screws that compress the ends of the C, exhibit anticlastic bending with parabolic intensities, allowing easy production of the two converging beams and adjustment of their trajectory angles. The merging crystal is made of a short silicon strip to optimize channeling deflection and Multiple Coulomb Scattering. The merging process may be applicable, for instance, in the injector of a muon collider, as the increase in beam intensity occurs over a short distance with a minimal rise in emittance.

Keywords: Accelerator Subsystems and Technologies; Accelerator Applications

*Corresponding author.

https://doi.org/10.1088/1748-0221/21/05/P05002

2026 JINST 21 P05002

Contents

2026 JINST 21 P05002

1 Introduction

The UA9 Collaboration has undertaken extensive investigations of the interactions between particles and crystals, leading to significant discoveries and innovative uses, all founded on developments of advanced equipment created and consistently improved over the past fifteen years [1, 2].

The latest proposed application is to demonstrate that two converging beams can be combined in a bent crystal to generate a resulting beam with an intensity near the sum of the incoming particles [3]. To demonstrate the feasibility of the proposed concept, the UA9 layout installation in the H8 beam line of the CERN-SPS North Area has been modified [4] as shown in figure 1. Two converging beams of positive hadrons are redirected from the main beam by two curved crystals. They may be combined in a third crystal positioned at their intersection, as schematically shown in figure 2. The three crystals serve to regulate the convergence angle of the two beams and to decrease the crystal bending angle needed for the merging process, thus lowering losses and the emittance rise during the passage through the merging crystal.

The merging process occurs as long as the angle of the converging beams closely aligns with the bending angle of the third crystal. The combined beam is nearly perpendicular to the exit face of the third crystal, and its phase space portrait closely resembles the side-by-side overlap of the phase space representations of the two converging beams. Essentially, the combining process results in the horizontal layering (stacking) of the two original beams.

The interactions influencing two-beam mixing in the third crystal involve planar channeling, volume reflection, and the amorphous phase. At the intersection of the two beams, the merging crystal named CR3 is positioned so that Beam 2 intersects it in channeling orientation, whereas Beam 1 moves tangentially to the end of CR3. Minor variations in the crossing angle are expected to greatly change the coalescence regime, as the two beams will impact distinct areas of CR3 and lead to a diverse distribution of the emitted particles. One of the objectives of the final experiment is to examine the different coalescing regimes. The capability to regulate the bending angles of the first two crystals should greatly assist this study.

Positively charged particles approaching highly pure crystalline materials at a small angle (θ) relative to the crystalline structure can become confined in planar channeling states between two neighboring crystalline planes. The critical angle that distinguishes the stable confinement region from the onset of de-confinement is $\theta_c = \sqrt{2U_{max}/pv}$, which depends on U_{max}, the potential well between

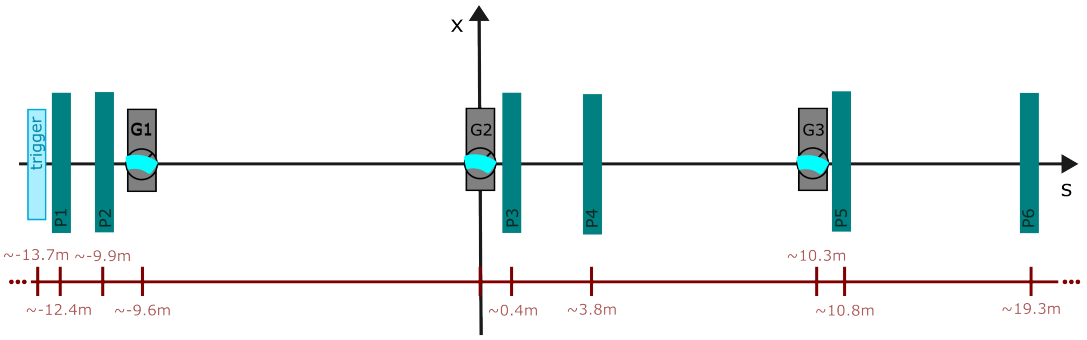

Figure 1. UA9 layout of the H8 experimental area for the merging test. There are six silicon microstrip stations (green boxes P1 to P6), with the trigger (light blue box), and three goniometer assemblies (black boxes G1 to G3 hosting the three bent crystals in light blue). The longitudinal distances from the central goniometer are shown on the bottom red line.

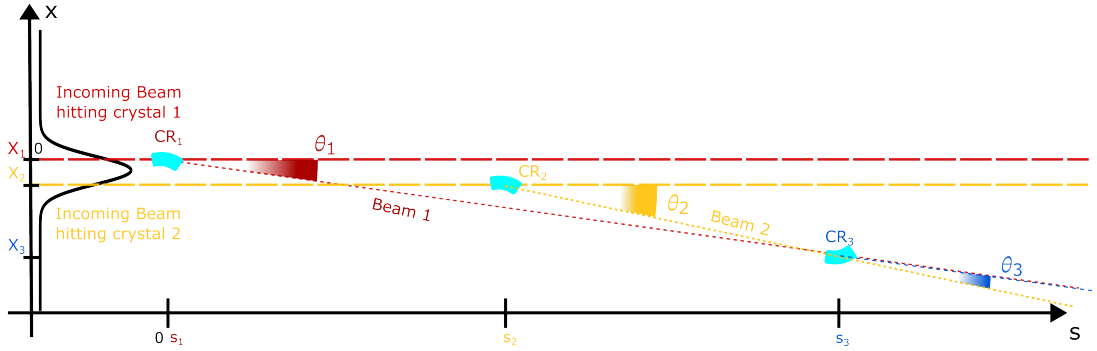

Figure 2. Schematic beam trajectories during the mixing test. Two upstream crystals (CR_1 and CR_2) extract, by means of channeling, two beams (Beam 1 and Beam 2) from the main flux of particles flowing in H8. Their deflection angles (θ_1 and θ_2) are chosen in order to cross at the longitudinal location of the merging crystal (CR_3). The merging condition requires that $\theta_3 = \theta_2 - \theta_1$.

two crystalline planes (~20 eV for Si (110) planes) and on p and v, the particle momentum and velocity respectively [5]. Channeling can be exploited in bent crystals when their bending radius (R) is larger than the critical radius ($R_c = pv/eE_c$, where E_c is the electric field intensity at the boundary of the stable trajectory region) [6]. The trajectory of the channeled particles is deflected by the same angle of the crystal bending $\theta_b = l/R$, where l is the crystal length. Particles entering a bent crystal at an angle θ slightly larger than θ_c can be deflected through volume reflection (VR) [5] mechanisms. In VR, particles reflect out of the curvature when they are nearly parallel to the planes, at the tangent point of the incoming trajectory with the arc of the crystalline planes. For Si(110), $\theta_{VR} \approx 1.3 \times \theta_c$. Particles approaching the crystal in the amorphous (AM) regime, i.e. with $\theta \gg \theta_c$, undergo no significant deflection but their angular spread increases because of Multiple Coulomb Scattering (MCS).

In this document, we describe the crystals and emphasize their functional properties to illustrate the practicality and the key characteristics of the two-beam merging procedure. The crystal characterization occurs through two methods: a beam based method, as detailed in refs. [7–9], and an optical method utilizing auto-collimators, briefly described in section 3. Switching between the two methods will save beam time and facilitate verification of the auto-collimator performance.

2026 JINST 21 P05002

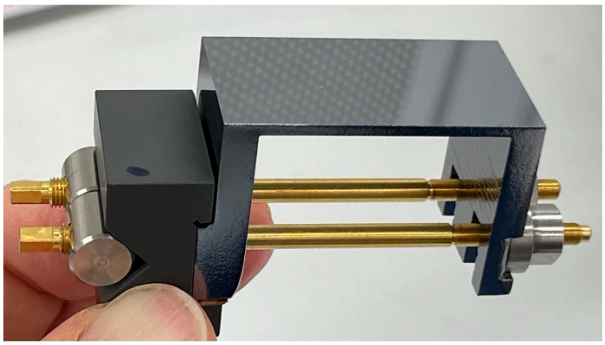

Figure 3. The RD22-1, representing the RD22-series of crystals for merging experiments.

2 Crystals for the merging test

In the merging tests, we utilize crystals from two distinct series, referred to as RD22 and ACP. The former is utilized to create and direct the two converging beams by guiding channeling deflection from the primary beam. The latter series is utilized for the actual merging process.

The crystals in the RD22 series belong to a unique class of relatively large silicon crystals resembling a C, curved by two screws that compress the ends of the C together, as illustrated in figure 3. They were designed in the 1990s for crystal extraction at the CERN-SPS synchrotron [10]. Their initial purpose was to produce a primary bend of a quasi-circular form, potentially free of anticlastic irregularities. To achieve this, ribs were constructed in the rear of the bent surface, according to a recognized method used in synchrotron light experiments — see for example [11, 12]. The UA9 collaboration recreated them without the ribs to utilize the anticlastic curvature. Four crystals of this kind, designated RD22-1 through RD22-4, were produced and tested. For each of them, the measurements of the curved surface $L_Y \times L_Z$ are $44 \times 22\,\mathrm{mm}^2$, with a thickness L_X of 1.5 mm. The crystal RD22-1 was broken during a mechanical stiffness examination at the manufacturer's location. The anticlastic curvature at the center of the crystal's vertical axis was noted as the compression at the C-ends was raised. The outcome is displayed in figure 4: on the left side, the anticlastic curvature, measured using an AltiSurf 520 optical sensor, is displayed for progressively tighter screw adjustments. On the right side, the fragments of the crystal are displayed: the fracture occurred abruptly for an anticlastic curvature ranging between 1860 µrad and 2000 µrad.

The crystals of the ACP series, used for the merging process, consist of a silicon strip housed in a titanium C-frame. Originally conceived for collimation tests in the SPS, the dimensions of the curved surface $L_Y \times L_Z$ are $50 \times 4\,\mathrm{mm}^2$, and the thickness L_X measures 3.0 mm. They are optimized for efficient channeling and for reduced Multiple Coulomb Scattering, thus ideal for the merging tests. The only sample used in our merging tests is the ACP83, shown in figure 5.

The measured values of the mechanical sizes of the RD22 and of the ACP series of crystals are shown in table 1. The values of the bending angle θ_b and of the bending radius R, measured along the vertical axis L_Y and at its mid-point, are discussed in sections 3 and 4.

In the merging tests, we initially used the set of crystals RD22-2, RD22-3, and ACP83, which was later substituted by the set RD22-3, RD22-4, and ACP83. In the diagram illustrating the particle trajectories in figure 2, the trio of crystals is labeled as CR1, CR2, and CR3, correspondingly, according to the position in the arrangement.

2026 JINST 21 P05002

Table 1. Parameters of the crystals: physical dimensions (L_X, L_Y, L_Z).

Crystal Name	L_X mm	L_Y mm	L_Z mm
RD22	1.50 ± 0.02	44.00 ± 0.02	22.00 ± 0.02
ACP83	1.00 ± 0.02	50.00 ± 0.10	4.00 ± 0.02

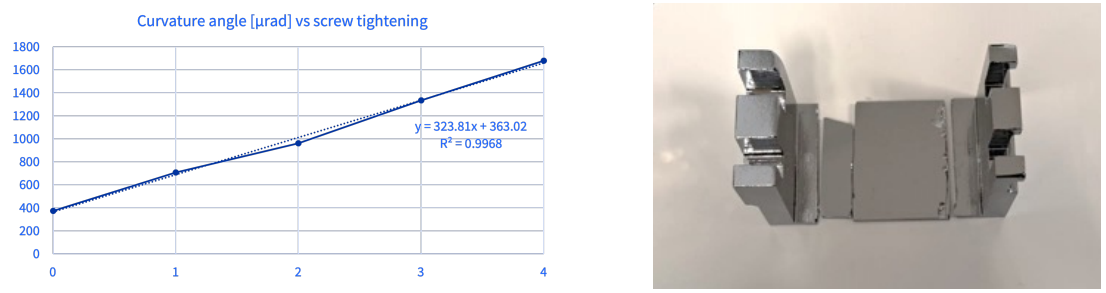

(a) RD22-1 anticlastic curvature. The value of 1 corresponds to a 1/4 screw turn.

(b) Broken RD22-1 crystal. The breaking point was between 1700 µrad and 2000 µrad

Figure 4. Test of the mechanical strength of the RD22-1 crystal. The anticlastic curvature was assessed in the crystal center using an AltiSurf 520 device at the location of the crystal manufacturer

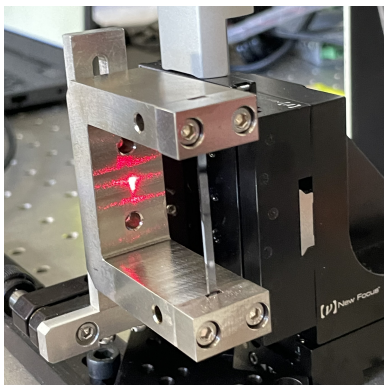

Figure 5. The ACP83, representing the ACP-series of crystals for merging experiments.

The RD22 crystal pair is used to guide primary particles into channeling states, producing beam 1 and beam 2, respectively. The crystal ACP83 is where the merging process happens. In the three crystals, we apply a primary bending curvature θ_p along the vertical axis, which leads to an anticlastic horizontal curvature θ_b on the $L_Y \times L_Z$ surface, aligned with the (110) crystalline planes used for channeling, while the L_Z axis runs parallel to the [001] crystalline axis. Figures 6(a), 6(b), and 6(c) illustrate a set of three crystals arranged inside the respective angular actuator located in the H8 region.

The crystal properties are evaluated through interactions with the primary beam particles and through the use of auto-collimators. Optical assessments are performed with both standard and specially designed auto-collimators. They facilitate the analysis of the elastic response to bending forces impacting the crystals and quantifying the bending angle related to a particular torque. The tests on the beam are performed using the telescopic apparatus shown in figure 1. We apply the

2026 JINST 21 P05002

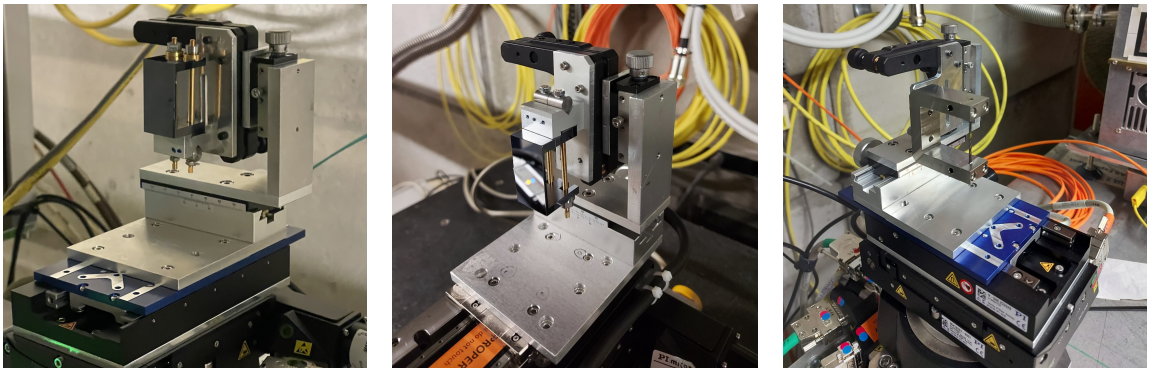

(a) RD22-2: C-shape crystal.

(b) RD22-3: C-shape crystal.

(c) ACP83: strip crystal with C-shape holder.

Figure 6. C-shape crystals RD22-2 (6(a)) and RD22-3 (6(b)) mounted on the upstream and central goniometers, respectively. ACP83 (6(c)), anticlastic crystal, is mounted on the downstream goniometer.

techniques described in refs. [8, 9] to obtain the bending angle measurements in channeling orientation and the vertical twist. Furthermore, we evaluate the transport efficiencies through the crystals in both channeling and Volume Reflection modes.

3 Measurements with the auto-collimators

Auto-collimators are optical instruments used for precise measurement of angular displacements. The concept upon which they rely is illustrated in figure 7. On the left, the light from point O is collimated by a high-quality objective lens, producing a parallel beam that strikes a flat, reflective surface at a right angle, reflects back along its original path, and converges at the origin point O. On the right, when the reflective surface tilts at an angle θ, the beam that is reflected shifts by an angle of $2 \times \theta$, causing the image to be laterally displaced from the origin point O. The displacement is $d = 2 \times \theta \times f$, where f signifies the focal length of the lens and θ indicates the tilt angle measured in radians. Since f is a specified constant for the auto-collimator, ascertaining the displacement d allows computation of the tilt angle θ [13].

Evaluating the curvature of a bent crystal is more intricate, as the light illuminates the whole crystal surface or at least a large fraction of it, and the back-reflected rays are captured by a significantly larger portion of the camera's sensitive area integrated into the device.

An example of this is illustrated in figure 8, where the crystal, shown as the gray shape, is presumed to be reflective with a constant radius of curvature and no surface imperfections. In figure 8(a), the trajectory of an individual ray of light is depicted, in order to establish the connection between the observed angular displacement θ_{meas} and the lateral shift h of the ray hit point from the Z-axis, which is

$$h = R \sin\theta = R \sin\left(\frac{\theta_{\text{meas}}}{2}\right) \Rightarrow \theta_{\text{meas}} \approx 2\,\frac{h}{R} + \frac{1}{3}\left(\frac{h}{R}\right)^3 + O\left(\frac{h}{R}\right)^5 . \tag{3.1}$$

To determine the bending angle, one may begin at one side of the crystal and extend to the opposite side, noting the measurement at every step (which relates to the offset h), as illustrated in figure 8(b). After different values of θ_{meas} have been acquired for various h, the data can be interpolated with a polynomial function of order 3, whose coefficient should be compared with those

2026 JINST 21 P05002

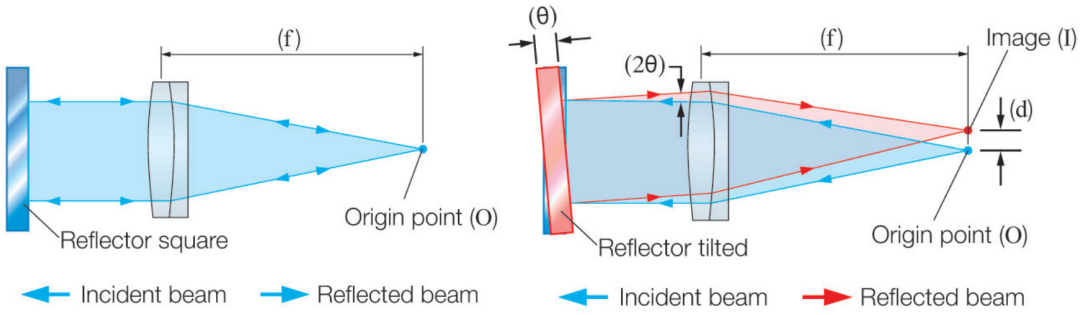

Figure 7. Working principle of an auto-collimator. *Left:* a perpendicular surface reflects the incoming parallel beam such that the incoming and reflected beams overlap. *Right:* for a surface tilted by an angle θ, the reflected image is reconstructed and displaced by an amount d. Reproduced with permission from [13].

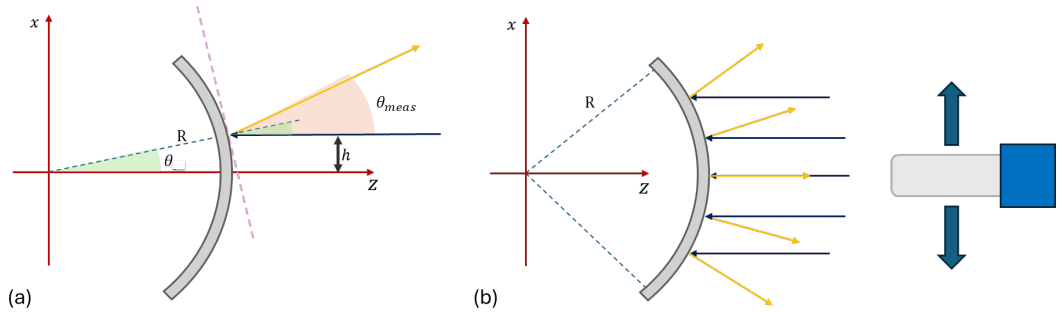

Figure 8. *(a)* Reflection of light on a curved surface at a specific point. *(b)* Measurement of a long bent crystal by scanning across its entire length.

of the approximated formula in 3.1. The interpolation method is effective even when the reflected light does not completely enter the auto-collimator, which typically happens in the situation of a large bending angle, such as the primary curvature.

The most practical way to collect the data consists in using a small window to isolate only a portion of the crystal. By moving this window in fixed steps, it is possible to scan different sections of the crystal and determine the curvature at specific points. Once the central point is identified, the change in angle can be evaluated by shifting the window position even just one step.

The advanced methods utilized to improve the resolution measurement of h and to enlarge the detected value of θ are thoroughly detailed in refs. [14], although they remain unpublished.

Angular measurements taken with auto-collimators on the crystals RD22-3 and RD22-4 are shown in figure 9. In both cases, the anticlastic curvature θ_b is illustrated as a function of the illuminated crystal slice along the vertical position. The significant observation is that the value of θ_b shows a parabolic shape, which, in the considered configurations, starts close to zero at the crystal's edge and reaches approximately 840 µrad near the center of its vertical axis. The red parabolic fits depicted in figure 9 closely align with the data in a highly accurate manner.

The observation of the gradient of θ_b versus Y in not totally unexpected. At the edges of the curved surface $L_Y \times L_Z$, where the legs are located, the mechanical stiffness is significant and the anticlastic bending is nearly absent. As one moves toward the crystal center, the anticlastic flexure gradually increases until it reaches its peak, located near the crystal center. The absence of an anticlastic

2026 JINST 21 P05002

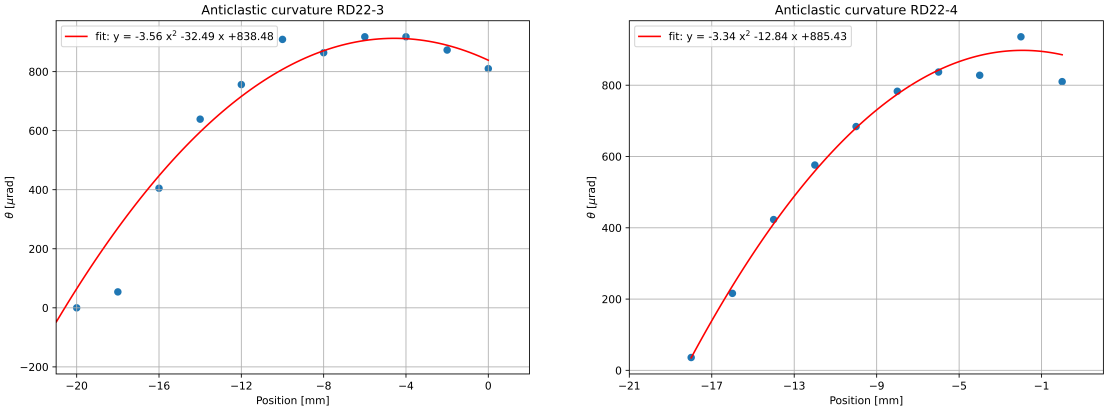

(a) RD22-3 curvature

(b) RD22-4 curvature

Figure 9. Auto-collimator measurements of the anticlastic curvature of the RD22-3 and RD22-4 crystals: the shape of θ_b is shown as a function of the position of the light hit-point.

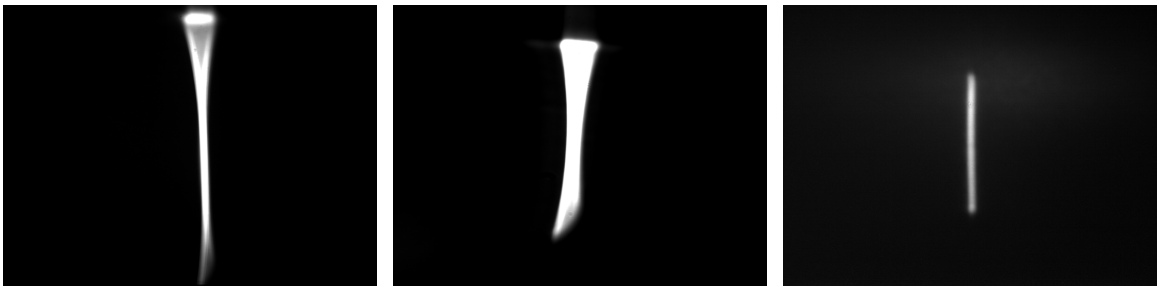

(a) Crystal RD22-3.

(b) Crystal RD22-4.

(c) Crystal ACP83.

Figure 10. Images captured by the auto-collimator camera.

curvature plateau is perplexing and indicates that the crystal's vertical height is insufficient to attain the balance of shear stress generated by the torque. Simulations will be initiated to verify our observations.

Extensive investigations were performed to optimize the anticlastic curvature gradient for merging tests. This procedure involved the previously mentioned destructive examination of the RD22-1 crystal to determine its failure threshold.

The images taken by the auto-collimator camera, produced by illuminating the crystals RD22-3, RD22-4, and ACP83, are shown in figure 10. The vertical axis shows the angular deviation caused by the main bending, while the horizontal span reflects the anticlastic curvature. The existence of an anticlastic gradient in the crystals RD22-3 and RD22-4 causes the images in figures 10(a) and 10(b) to take on a sand-clock shape. This information has been employed to generate the outcomes shown in figure 9.

Examining figure 10(c), it is evident that there is no anticlastic gradient in the crystal ACP83. The main bending, established by scanning the crystal using a horizontally oriented mask, is $\theta_p = 5.08$ mrad. The anticlastic curvature, defined by the extent of the brightness zone along the horizontal axis, is $\theta_b = 171$ µrad.

Angular measurements of curved crystals using an auto-collimator are unprecedented within this parameter range. The achieved precision is of about 5 µrad. Essential measures for this performance include enhancing the quality of the polished bent surface to boost reflectivity and automating the data collection process, which has demonstrated to improve the resolution by a factor of about 4.

2026 JINST 21 P05002

4 Measurements with beam

Single crystal parameters are measured by irradiating it with a 180 GeV hadron beam in the H8 beamline of the SPS North Area, using the sensors and goniometers displayed in figure 1 for the real-time track reconstruction. The process necessitates tailoring the data acquisition software to the combination of crystals, goniometer, and sensors chosen by the user prior to each acquisition. A minimum of four stations must be chosen: two for detecting each group of incoming or outgoing particle tracks impacting the crystal being studied. The DAQ software is customized to accommodate a diverse range of configurations. The real time and the generated scatter plot closely resemble those detailed in ref. [8].

To maintain brevity, we focus on characteristics of the RD22-4 crystal, illustrated in figure 9. The crystal RD22-2 and RD22-3 have a very similar behavior. The graph in figure 11(a) illustrates the value of the anticlastic curvature measured with beam versus the vertical hit-point of the beam particle paths. The graph is generated by combining the data from 5 runs, with each run consisting of approximately 16 million events. Prior to each run, the crystal center was adjusted vertically by 3 mm, resulting in a vertical range of approximately ±7.5 mm around the anticlastic peak. The red curve represents the parabolic interpolation of the displayed data. The graph in figure 11(b) indicates that the interpolating parabolas for the two data sets gathered with the beam (blue curve) and the auto-collimator (green curve) are nearly identical.

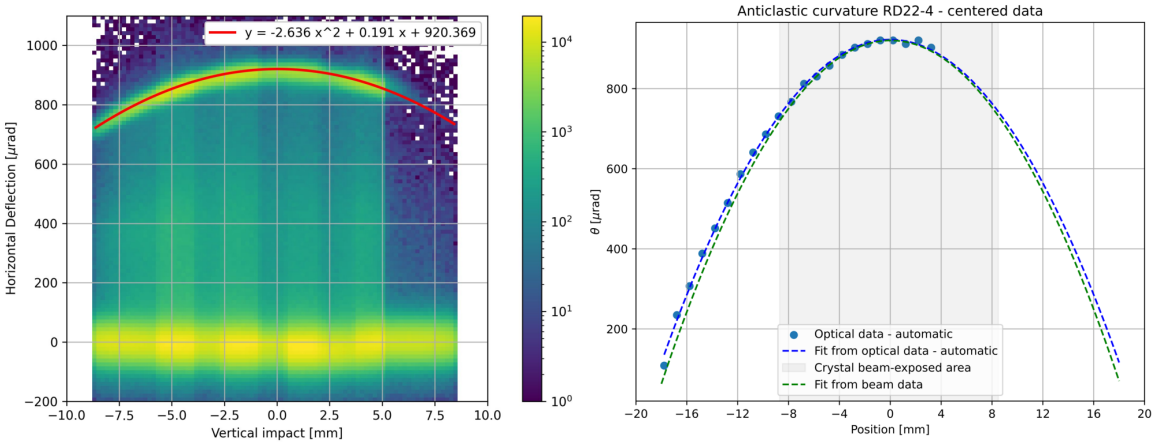

(a) RD22-4 curvature measured with beam (b) RD22-4 curvature measured with the auto-collimator

Figure 11. Anticlastic curvature of the RD22-4 crystal versus the vertical coordinate.

The crystal ACP83 has undergone multiple measurements with a beam. We present in figure 12 the information gathered during a high statistics run comprising approximately 16 million events. In figure 12(a), the deflection of the track is graphed against the incoming angle. The graph distinctly displays the channeled particles at the top, the particles not captured in channeling states at the bottom, and the ensemble of dechanneled particles in the middle. The red dots indicate the barycenter of the deviated particles, whose contour is angled because of the residual torsion in the ACP83 crystal. The histogram of track deflection is displayed in figure 12(b). The set of values around zero represents the particles not captured in channeling states, only perturbed by MCS during the crystal traversal. The values ranging around 184 μrad refers to the channeled set of particles.

2026 JINST 21 P05002

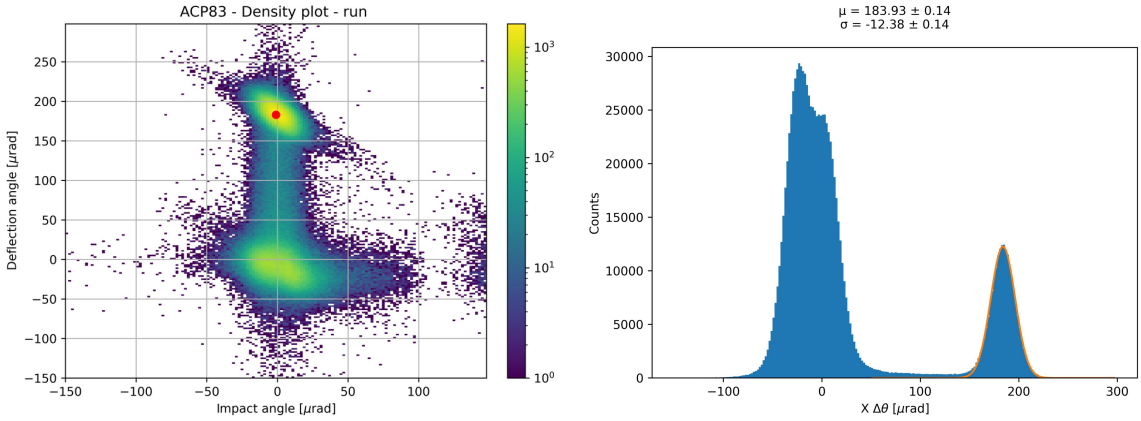

(a) Plot of the track deflections versus the impact angle (b) Histogram of the track deflections

Figure 12. Measurement of the ACP83 crystal with beam: 16 million events are collected and plotted.

Analogous graphs are displayed in figure 13 for the crystal RD22-4. Throughout the data collection, the primary beam struck the crystal at the central vertical position. To keep it simple, we exclude similar graphs relating to particles in VR or in amorphous orientation.

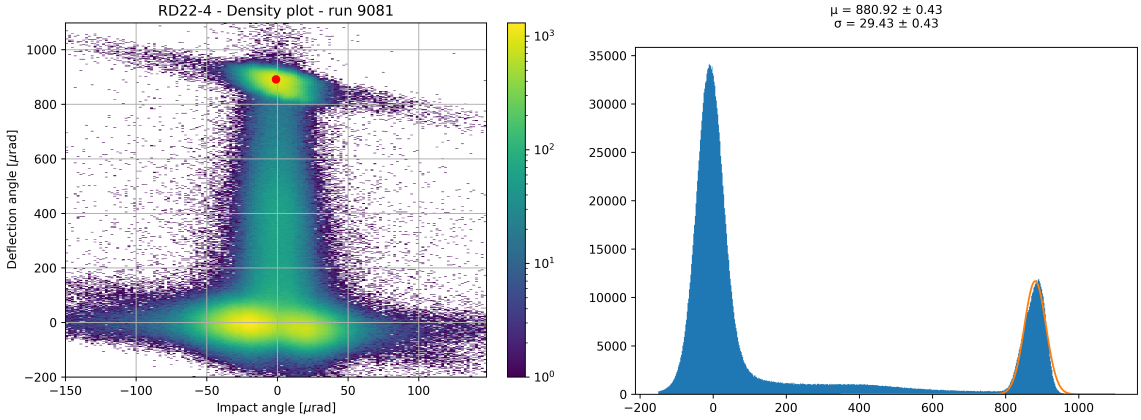

(a) Plot of the track deflections versus the impact angle (b) Histogram of the track deflections

Figure 13. Measurement of the RD22-4 crystal with beam: 16 million events are collected and plotted.

With these plots, it's possible to identify crystal characteristics, such as θ_b, vertical torsion, channeling, and VR efficiencies.

The RD22-4 crystal, representing the RD22 crystal class, and the ACP83's performance are displayed in tables 2 and 3. The RD22-4 performance is measured at the pick value of the anticlastic curvature. When shifted vertically, the bending angle θ_b should decrease and the channeling efficiency ϵ_c increase.

5 Conclusions

The crystals employed in the two-beam merging process are highly suited for ensuring the success of these tests. The RD22 series of crystals enables the extraction of the two converging beams from

2026 JINST 21 P05002

Table 2. Measured parameters of the crystals RD22-4 and ACP83: bending angle θ_b; residual torsion: t. Note that the anticlastic gradient prevent measuring t in the RD22-4.

Crystal Name	θ_b µrad	t µrad mm^{-1}
RD22-4	913.6 ± 0.1	–
ACP83	183.9 ± 0.1	0.75 ± 0.15

Table 3. Performance of the crystals RD22-4 and ACP83: ϵ_{CH} represents the CH efficiency, ϵ_{VR} denotes the VR efficiency, and $(\sigma_{\theta_{\mathrm{out}}}/\sigma_{\theta_{\mathrm{in}}})_{\mathrm{AM}}$ and $(\sigma_{\theta_{\mathrm{out}}}/\sigma_{\theta_{\mathrm{in}}})_{\mathrm{VR}}$ indicate the increase in beam divergence in AM and VR orientations, respectively. The selected range of θ, the angle of the incoming particle, is shown in each column of the table.

Crystal	ϵ_{CH} $\theta \le \theta_c$	ϵ_{CH} $\theta \le \theta_c/2$	ϵ_{VR} $2\theta_c \le \theta \le 3\theta_c$	$(\sigma_{\theta_{\mathrm{out}}}/\sigma_{\theta_{\mathrm{in}}})_{\mathrm{AM}}$ $-5\theta_c \le \theta \le -4\theta_c$	$(\sigma_{\theta_{\mathrm{out}}}/\sigma_{\theta_{\mathrm{in}}})_{\mathrm{VR}}$ $2\theta_c \le \theta \le 3\theta_c$
RD22-4	(37.2 ± 0.4) %	(37.0 ± 0.4) %	(93.3 ± 0.1) %	1.87 ± 0.02	1.92 ± 0.01
ACP83	(53.40 ± 0.43) %	(55.8 ± 0.3) %	(92.3 ± 0.1) %	1.21 ± 0.02	1.33 ± 0.03

the primary particle flow with quite good efficiency. Additionally, they allow for a simple and swift modification of the trajectory angles to meet the limitations set by the CR3 curvature.

We utilized two separate approaches, one relying on beam interactions and the other on the use of an auto-collimator, to assess certain important parameters of the crystals.

The plan is now to collect merging data in the H8 beam and analyze it. Further studies on the characteristics of the C-shaped crystals could enhance comprehension of the significant anticlastic curvature change related to the crystal structure.

Acknowledgments

The authors would like to acknowledge the continuous support of our funding agencies. Special thanks are due to Maarten Van Dijk and Laurie Nevay of the BE-EA-LE for excellent coordination of the H8 beam line at CERN.

Data Availability Statement. This article has no associated data or the data will not be deposited.

References

[1] W. Scandale et al., *Feasibility of crystal-assisted collimation in the CERN accelerator complex*, *Int. J. Mod. Phys. A* **37** (2022) 2230004.

[2] W. Scandale and A.M. Taratin, *Channeling and volume reflection of high-energy charged particles in short bent crystals. Crystal assisted collimation of the accelerator beam halo*, *Phys. Rept.* **815** (2019) 1.

[3] W. Scandale et al., *Beam merging assisted by a bent crystal*, *Eur. Phys. J. Plus.* **138** (2023) 981.

[4] W. Scandale et al., *UA9 apparatus for testing beam merging*, 2025 *JINST* **20** P10049.

[5] A.M. Taratin, *Particle channeling in a bent crystal*, *Phys. Part. Nucl.* **29** (1998) 437.

[6] V.M. Biryukov, Y.A. Chesnokov and V.I. Kotov, *Crystal channeling and its application at high-energy accelerators*, Springer Science & Business Media (1997).

2026 JINST 21 P05002

[7] G. Hall et al., *A high angular resolution silicon microstrip telescope for crystal channeling studies*, *Nucl. Instrum. Meth. A* **924** (2019) 394.

[8] R. Rossi et al., *Track reconstruction of particle interactions in long crystals with large bending*, 2021 *JINST* **16** P05017.

[9] R. Rossi et al., *Track reconstruction and analysis of particle interactions in short bent crystals*, 2023 *JINST* **18** P06027.

[10] RD22 collaboration, *Proton extraction from the SPS with a bent crystal*, *Nucl. Instrum. Meth. A* **351** (1994) 183.

[11] C.J. Sparks, G.E. Ice, J. Wong and B.W. Batterman, *Sagittal focusing of synchrotron x-radiation with curved crystals*, *Nucl. Instrum. Meth.* **195** (1982) 73.

[12] L. Feng et al., *Evaluation of two methods to minimize the anticlastic curvature of cylindrical bent crystals*, *J. Synchrotron Radiat.* **15** (2008) 140.

[13] T.M. Experts, *Autocollimators and accessories*, https://www.taylor-hobson.com.

[14] W. Scandale et al., *Bent crystal characterization from Autocollimator measurements*, 2026 *JINST* **21** P03026.

2026 JINST 21 P05002